

CHEMICAL THERMODYNAMICS
AND THERMOCHEMISTRY

Enhanced Mechanical Properties of Sintered Iron via Cyclic Induction Heat Treatment

Yifei Chen^a, Runjian Jiang^a, Chengsong Zhang^a, Dazhi Chen^a, and Guodong Cui^{a,*}

^a*School of Materials Science and Engineering, Southwest Jiaotong University, Chengdu, 610031 China*

**e-mail: gdcui@swjtu.edu.cn*

Received December 28, 2019; revised December 28, 2019; accepted March 11, 2020

Abstract—In order to improve the mechanical properties of sintered iron, the cyclic induction heat treatment (CIHT) was applied to produce ultrafine microstructure on surface. The surface microstructure of refined grains and micropores, and the related mechanical properties were investigated. Results indicated that the refined grain (24.60–3.66 μm) and micropore (9.52–1.67 μm) contribute to a substantial improvement in compressive yield strength (177–555 MPa) and surface microhardness (123.0–300.8 $\text{HV}_{0.1}$) of the sintered iron samples. Grain refinement was ascribed to the high nucleation rate and short grain growth time, which is due to rapid processing and a large number of microporous interfaces. Meanwhile, the micropore structure was refined due to grain refinement in resintering process. Thus, the CIHT is considered as a feasible method to improve mechanical properties of iron-based sintered alloys, providing them with more promising applications on key structural parts.

Keywords: surface strengthening, cyclic induction heat treatment, sintered iron, ultrafine microstructure

DOI: 10.1134/S0036024420130075

1. INTRODUCTION

As an important way to improve the surface properties of sintered iron, surface strengthening can enhance the microhardness, yield strength and fatigue life of the parts [1–3]. Lamim et al. [4] had researched the duplex surface treatment of sintered iron by plasma nitriding and plasma carburizing at low temperature, and the results shown that the surface microhardness has been enhanced significantly. Cui et al. [5] fabricated sintered iron by spark plasma sintering (SPS). The strength of sintered iron was enhanced by quenching after carburization. It obtained a higher yield strength level (256 MPa), which has increased by 90% comparing non-treated sintered iron. Bendo et al. [6] studied the nitriding of surface Mo-enriched sintered iron. Their results show that surface nitriding of Mo-enriched sintered iron leads to the formation of a composite layer with different morphology depending on the nitriding temperature. The microhardness was also improved significantly. Although the research above all has reported some progress in improving the performance of sintered iron, they still don't get enough mechanical properties to solve the problem of applying sintered iron to key components. Compared to other surface strengthening technologies, IHC has many advantages including low cost, energy saving, high production efficiency and no pollution [7, 8]. IHC can refine grains and micropores at the same time, which optimizes the microstructure of sintered

iron [9–11]. What is more, CIHT is a more effective way to refine the surface grains via repeated heat treatment, which has more advantages than IHC [12–14]. Although CIHT is considered an effective method to improve properties, the effect of CIHT on the properties of sintered iron has not been reported.

In this paper, in order to improve the mechanical properties of sintered iron, its surface modification was conducted by using CIHT method. The purpose of this work is to improve surface microstructure by CIHT, so as to improve its properties. The effects of CIHT on microstructure and mechanical behavior of sintered iron have been investigated and analyzed in detail.

2. EXPERIMENTAL

The Fe–N powder (~300 nm) was synthesized at 650°C for 2 h using ammonia reduction and nitridation of a commercial iron oxide powder [15]. The schematic diagram is shown in Fig. 1a. The ultra-fine Fe–N powders were packed in graphite mold (30 mm in diameter, 60 mm in height, and 10 mm in inner diameter) and compacted under a load of 51.9 MPa (0.6 t) to get green compact. The graphite mold with Fe–N powders was put into a stainless steels cylinder and was buried in carbon powder, aiming at preventing the graphite mold and specimen from being oxidized. The specimens were sintered in the high-temperature box resistance furnace (KSY-12D-18, Shenyang

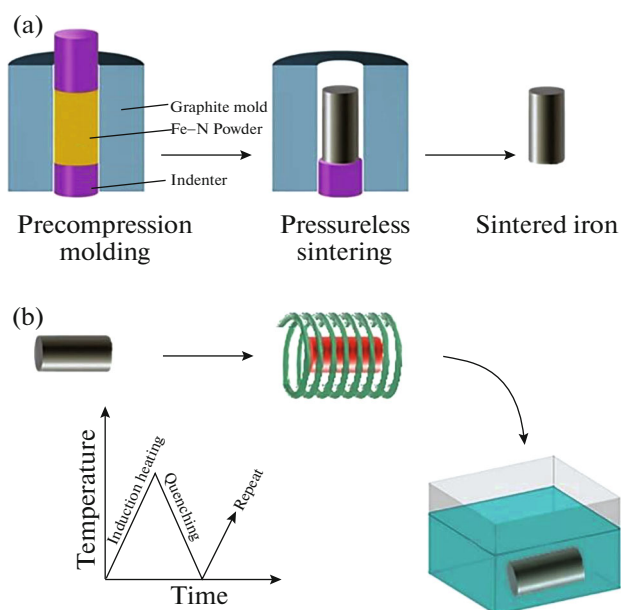


Fig. 1. Schematic illustration of (a) pressureless sintering and (b) cyclic induction heat treatment.

Jieneng Electric Furnace Factory, China) in atmospheric environment. They were placed in the furnace when the temperature of the furnace rises to 1100°C. The specimens were quickly warmed from room temperature to 1100°C. After a holding of 30 min, the specimens were taken out from the furnace chamber and underwent air cooling. The whole sintering process was under pressureless conditions, then specimens with a diameter of about 7 mm and a length of about 20 mm were prepared eventually.

The sintered iron samples were treated by CIHT. The schematic diagram is shown in Fig. 1b. The sintered iron samples were cut into cylinders of 7 × 20 mm. Then, the specimens were heated quickly in high-frequency induction hardening furnace (DSGP-80). The induction heat treatment was carried out using a 20 kHz frequency for 3–6 s on sintered iron specimens, which raised its outer periphery surface temperature to approximately 1210–1475 K; further quenching was carried out using water to increase the

case depth and hardness. Finally, the above steps were repeated by the designed time and numbers, which are listed in Table 1. The induction heating time and the number of cycles were varied to study the impacts of such variations on microstructure and properties. The optimized heating time and cycle number can be obtained by comparing the results.

2.1. Characterization Methods

The specimens (sintered iron) were grinded and ultrasonically cleaned to remove residual carbon paper. Specimens for laser confocal microscopy (VK9700 instrument) were prepared by polishing with abrasive paper, then they were etched with 4% nitric acid ethanol solution. The optical metallographic images of the specimens were obtained using Olympus GX51F microscope, Japan. The alloy components were measured by X-ray fluorescence spectrometry (XRF, X-MET7500, Oxford Instruments, UK). The Vickers hardness (HV) of specimens were measured with a digital micro hardness tester (HVS-1000, Laizhou Huayin Testing Instrument Co., Ltd, China) at a load of 100 gf and the pressing time of 15 s. The sintered specimens were cut into cylinders of 6 × 9 mm for compressive performance test on the electronic universal testing machine (WDW-200) with a strain rate of 1 mm/min at ambient temperature. The apparent yield properties were determined using the 0.2% offset method.

3. RESULTS AND DISCUSSION

3.1. Fe–N Powder and Sintered Iron

The synthetic process of Fe–N powders can be described by Eq. (1) [15]. The sintered iron samples were manufactured by pressureless sintering Fe–N powders at 1100°C. The Fe₃N powders are instable in high temperature environment, and the chemical reaction equation in the heating process is shown at Eq. (2) [15]. Then the Fe–N powders are decomposed completely during the sintering process at 1100°C as the reaction equation shown at Eq. (3). The X-ray diffraction patterns of Fe–N powder and sintered iron are shown in Fig. 2a. The main phase composition of the Fe–N powder as examined by XRD is ε-Fe₃N. The XRD diffraction patterns verify that the final sintering product is α-Fe

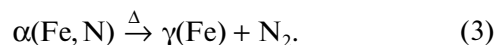
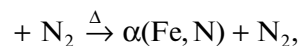
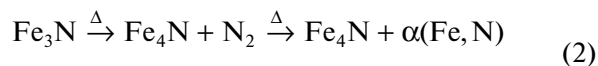


Figure 2b shows that microstructure of sintered iron consists of α-Fe matrix and residual pores. One can

Table 1. The different iron sintering processes

Specimen	Heating time, s	Number of cycles
RM	0	0
T3-N2	3	2
T3-N4	3	4
T3-N6	3	6
T4-N6	4	6
T5-N6	5	6
T6-N6	6	6

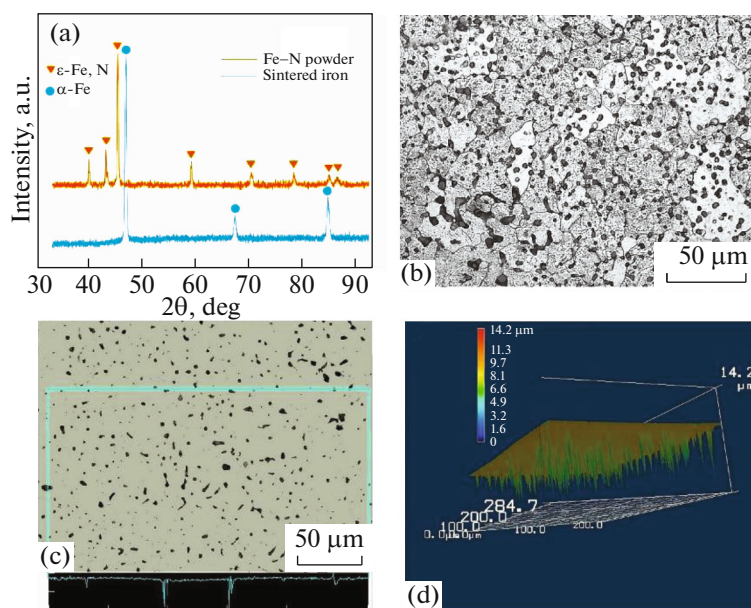


Fig. 2. The X-ray diffraction (XRD) patterns and the micromorphology of sintered iron. (a) XRD patterns of Fe–N powders and sintered iron; (b) metallographic structure; (c) is the micropores morphology; (d) 3D morphology of micropores.

see that many micropores are uniformly distributed on the grain boundaries and material matrix, but the size of micropores is inhomogeneous. In this study, based on the physical properties and microstructure, the decomposition and sintering process can be described as follows. Initially, a large number of α -Fe crystallites were formed due to the release of N_2 . These small α -Fe crystallites then grew or adhered together to form larger secondary aggregates. A part of micropores formed during the decomposition of Fe_3N phase due to emission of nitrogen gas. Another part of the micropores formed during the sintering process, the sintering neck growth is the reason of retained micropores forming. But with the grain growth, grain boundary moving through micropores causing a large number of pores to disappear [16, 17]. The micropores are characterized in Fig. 2d, and many micropores of different heights are described by 3D morphology with different colors. The depth statistics from Fig. 2d show the average size of micropore is $9.52 \mu m$. As shown in Fig. 2b, the grains size of sintered iron is calculated as $24.60 \mu m$ by using the straight-line intersection method given in Chinese standard (no. GB/T6394-2017).

3.2. Microstructure of Sintered Iron Processed by Cyclic Induction Heat Treatment

The typical optical micrographs of sintered iron processed by CIHT at different number of cycles and same heating time are shown in Figs. 3a–3c. The microstructure consists of α -Fe matrix and micropores. For the specimens with different process param-

eters, as seen in Fig. 3, the microstructures exhibit similar characteristics in terms of ferrite grain size, micropores size and morphology. The optical images revealed that the size of surface grains is decreased by increasing the number of cycles, and they are all smaller than that of RM. The grain refinement is attributed to repeat phase transition during CIHT. The grain size is influenced by grain nucleation and growth [18, 19]. The grain can be refined by increasing nucleation rate and decreasing growth rate. Generally, the non-uniform nucleation mainly occurs in solid phase transition [20]. Induction hardening has the characteristics of fast heating, fast cooling and short holding time. Heating and cooling at higher speed can easily lead to greater superheating and undercooling [21, 22], which can increase nucleation rate. The grain growth time is short due to short holding time. The characteristic of non-uniform nucleation is that the nucleation location is the defect of solid phase [23]. Figure 3 shows that the many micron-sized pores uniformly present in the grain boundaries and material matrix. Thus, a large number of grain boundaries and microporous interfaces are the important reasons for the increase in nucleation rate. The above causes the increasing of nucleation rate and shorting grain growth time. Thus, the smaller grain can be obtained after CIHT. Besides, the treated specimens have more nucleation points due to the increasing of grain boundary and micropores interface, which leads to the treated specimens obtaining higher nucleation rate. This is also the reason why the grains are further refined after multiple cycles of treatment. Finally, the size of grains decreases with the increasing of number

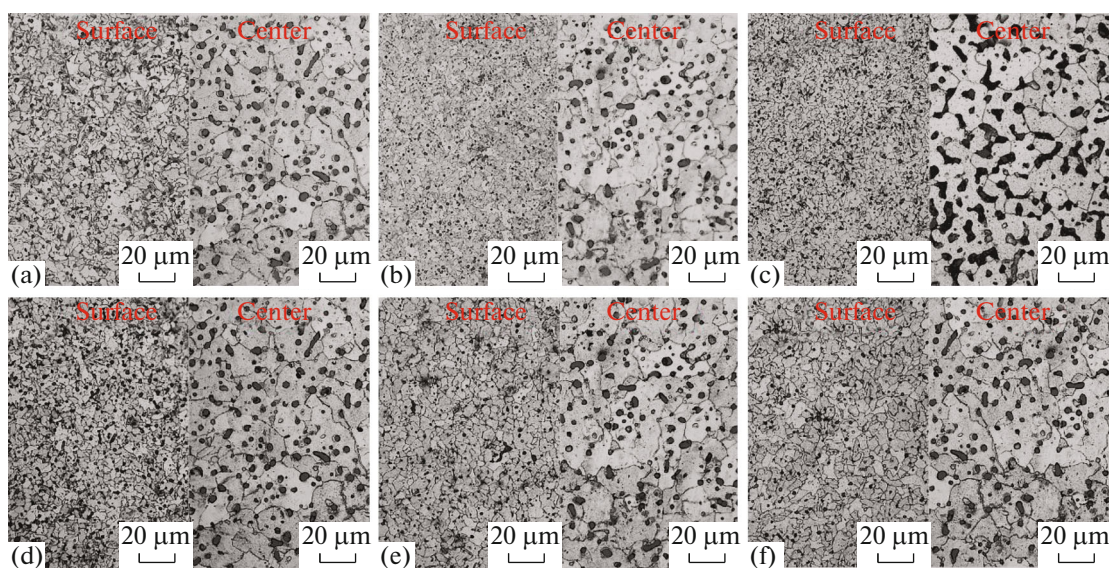


Fig. 3. The optical images of sintered iron showing microstructure of grains and micropores of (a) T3-N2, (b) T3-N4, (c) T3-N6, (d) T4-N6, (e) T5-N6, and (f) T6-N6.

of cycles due to repeated phase transformation. Figure 3 shows another phenomenon that the grain refinement efficiency decreases with the increasing of number of cycles. Thus, increasing the number of cycles will result in finer grains, but the refinement efficiency is not obvious. It should be noted that, comparing the microstructures of surface and center, a dramatic difference in micropore size is observed. The grain size in center is larger than that of surface in Fig. 3, and the microstructure is gradient structure of grain size on the surface.

The microstructure of the sintered iron, processed by CIHT at different heating time and same number of cycles, is shown in Figs. 3d–3f. The microstructure consists of α -Fe matrix and micropores. The optical images revealed that the surface grain is refined by decreasing the heating time. Long heating time causes higher temperature on surface, and higher temperature causes faster growth of grains due to higher atomic diffusion coefficient. In addition, long heating time also gives the grains more time to grow up. Thus, when the temperature higher than austenite transformation temperature, the specimens with lower temperature have smaller grain size.

Figures 4a–4c show the microstructure of surface micropores of sintered iron processed by different number of cycles. It can be seen that the micropore size is uniform, and the surface micropore size is decreased by increasing the number of cycles, and they all smaller than that of RM. In addition, Figs. 4d–4f show the microstructure of surface micropores of sintered iron processed by different heating time, and it shows a phenomenon that the surface micropore is refined by decreasing the heating time. The phenomenon indicates the proportional relationship between

the size of grains and micropores. The mechanism of micropore shrinkage has two ways. First, the vacancies around the pore diffuses to the grain boundaries through the bulk diffusion and are absorbed by them. The micropores shrink with the decreasing of vacancies. The final result is shrinkage of sintered iron. Second, the vacancies around the pores on the grain boundary diffuse along the grain boundary to both ends and disappear outside the sintered iron. The micropores also shrink with the decreasing of vacancies [17].

The reason of micropore refinement in sintering has been studied in great detail by German and Randall, and they put forward a formula as Eq. (4) about the relation of grain size and micropore size [24]:

$$d = G(\varepsilon/6)^{1/3}, \quad (4)$$

where ε is the fractional porosity, the grain diameter G and pore diameter d are related by this formula. The positive correlation between pore size and grain size can be observed at Fig. 5. The green point is calculated value, which is calculated from Eq. (4). The G and ε are obtained by experimental. The violet point is experimental value. Figure 5 shows that the calculated value is the same as the experimental value. The experimental model is suitable for the present experiment. Thus, the pores refinement is attributed to grain refinement in the resintering process.

3.3. Mechanical Properties of Sintered Iron Processed by Cyclic Induction Heat Treatment

The microhardness of specimens processed by different number of cycles is shown in Fig. 6a. The error is the standard deviation after averaging 5 measure-

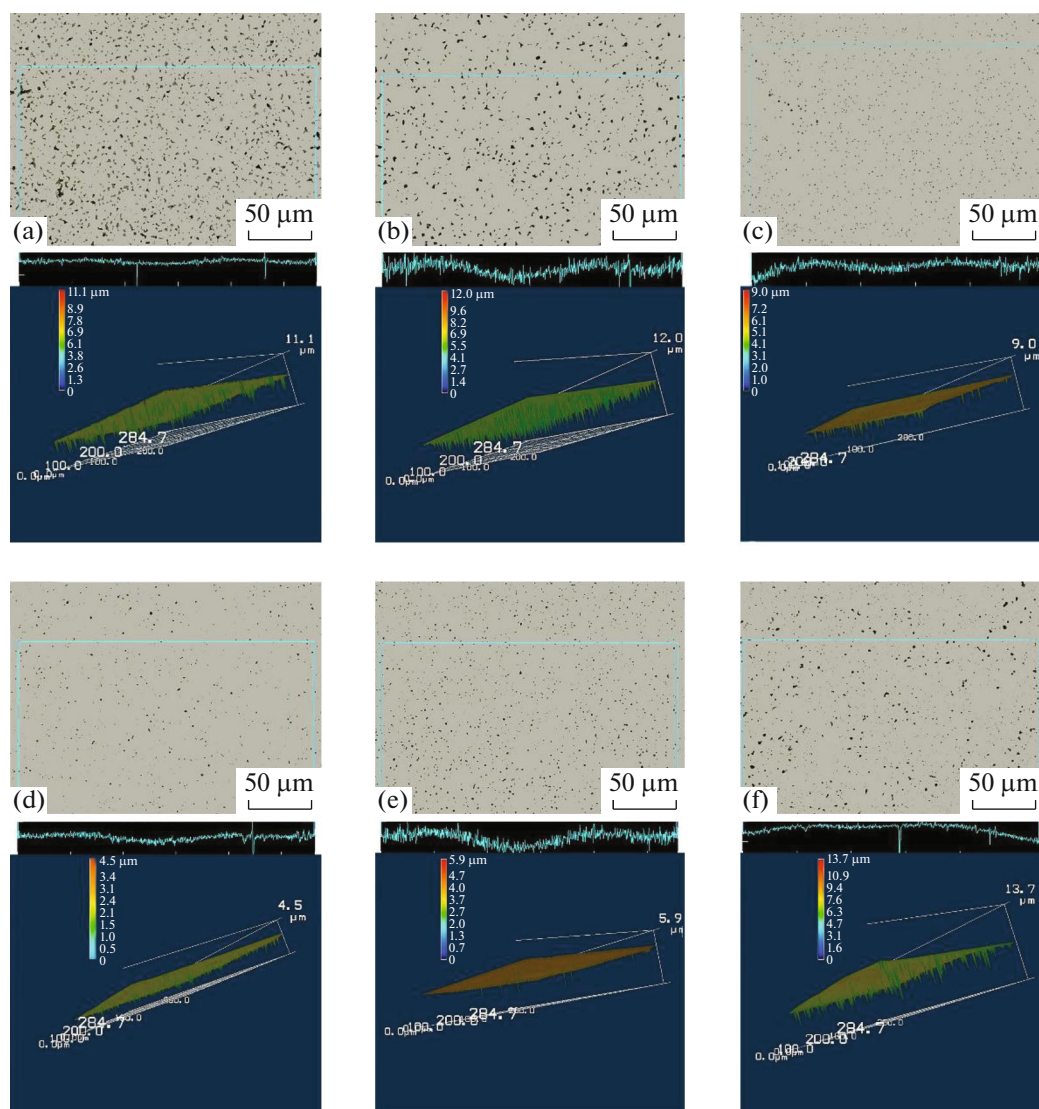


Fig. 4. The optical images and laser confocal images of sintered iron showing microstructure of surface micropores of (a) T3-N2, (b) T3-N4, (c) T3-N6, (d) T4-N6, (e) T5-N6, and (f) T6-N6.

ments selected randomly on the specimens. The microhardness appears a substantial promotion after CIHT. It can be seen that the microhardness of the specimens processed by CIHT was higher than that of RM. In addition, microhardness test results show that the surface hardness is increased by increasing the number of cycles, and the microhardness is gradual decreased from surface to center. The microhardness of the T3N6 sample decreases from 300.8 to 152.7 HV in the depth range from surface to center. This trend is mainly related to the surface grain size and the micropore size shown in Figs. 3 and 4. When the dislocations slip to grain boundaries and pore interface, it can form dislocation entanglement and hinder the slippage of dislocations, and therefore the specimens with smaller size of grains and micropores have higher

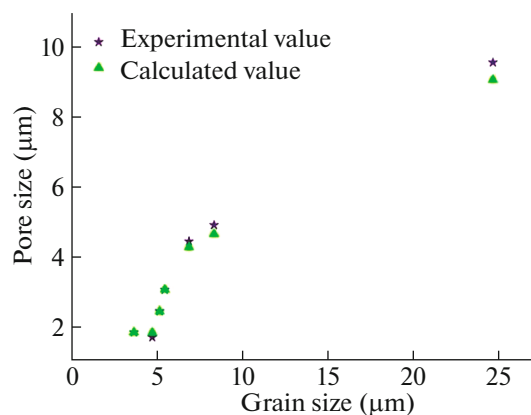


Fig. 5. Relationship of grain size and pore size.

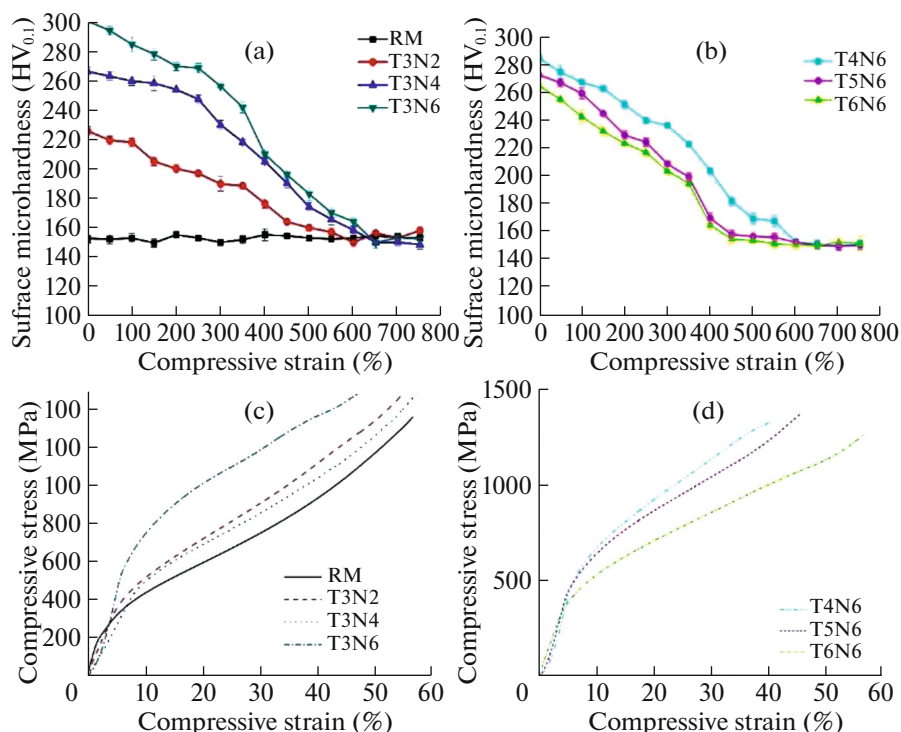


Fig. 6. Microhardness test of sintered iron processed by (a) different number of cycles and (b) different heating time; engineering stress-strain curves of sintered iron samples processed by (c) different number of cycles and (d) different heating time.

microhardness [25]. Figure 6b shows the microhardness comparison chart after the process of CIHT at different heating time and same number of cycles. The microhardness test results revealed that the sintered iron samples with short heating time have higher microhardness, and decreasing heating time is conducive to obtaining better hardness performance. This is because the less heating time causes the refinement of grains and micropores.

The selected compressive stress-strain curves of sintered iron samples processed by CIHT at different number of cycles and same heating time are illustrated in Fig. 6c, while the 0.2% offset yield strength for these four preparation conditions are compared as well. The sintered iron samples exhibit some typical mechanical behaviors including absence of distinct yield point and continuous yielding. The curves show that the yield strength increases with the increase in the number of cycles. It is because the dislocation slip causes plastic deformation of the specimens. When the specimens are exposed to external force, dislocation pile-up is occurred in grain boundaries and micropore interfaces, then the dislocation turn into fixed dislocation, and the fixed dislocations prevent dislocations from continuing to slip [26, 27]. Thus, the specimens with smaller grains and micropores have longer grain boundaries and micropore interfaces. Meanwhile, the longer grain boundaries and micropore interfaces cause higher microhardness and yield strength. In

addition, micropore is another important influence factor. When the dislocation passes the micropores, the micropores can block the motion of the dislocations and change the propagation direction [28]. Besides, for porous iron, deformation is accompanied by pore collapse, accordingly, the specimens with small and dispersed micropores have excellent microhardness and yield strength [29]. It can be seen from Fig. 6c that the yield strength increases with increase in the number of cycles. The specimen RM has the lowest yield strength (177 MPa). The specimen T3N6 has the highest yield strength (555 MPa), which is about three times as much as that of RM. Figure 6d shows the compressive stress-strain curves of sintered iron samples processed by different heating time and same number of cycles. It appears a phenomenon that the yield strength increases with the decreasing of heating time, which is also related to the grains and micropores refinement as mentioned above.

4. CONCLUSIONS

The present work has investigated and discussed the evolution of the surface ultrafine microstructure and related mechanical behavior of sintered iron, with a special emphasis on strengthening effects of refined grain and micropore. The sintered iron samples with different microstructure were prepared by CIHT. There are some major achievements in this paper that can be summarized as follows.

(1) The Fe–N powders are decomposed completely during pressureless sintering at 1100°C, and the microstructure of sintered iron consists of α -Fe matrix and residual micropores.

(2) The grains and micropores of sintered iron can be refined significantly by CIHT. Grain refinement was ascribed to the high nucleation rate and short grain growth time in phase transition. In addition, the micropores were refined due to grain refinement in resintering.

(3) Grain size gradient microstructure formed on the surface of the specimens treated by CIHT, which causes the microhardness of the specimens gradually decrease from the surface to the core.

(4) The microhardness and yield strength are improved significantly due to grains and micropores refinement. The optimal process is T3N6 in this paper, the smallest size of grains and micropores are 3.66 and 1.672 μm , and the highest surface microhardness and yield strength are 300.8 $\text{HV}_{0.1}$ and 555 MPa.

FUNDING

This work was Supported by Sichuan Education Reform Project (no. JG2018-158) and National Natural Science Foundation of China (grant nos. 51601156, 51601117, and U1537201).

REFERENCES

1. S. W. Xia, Y. Liu, D. M. Fu, B. Jin, and J. Lu, *J. Mater. Sci. Technol.* **32**, 1245 (2016).
2. H. W. Huang, Z. B. Wang, J. Lu, and K. Lu, *Acta Mater.* **87**, 150 (2015).
3. V. Llana and F. J. Belzunce, *Appl. Surf. Sci.* **356**, 918 (2015).
4. T. S. Lamim, E. A. Bernardelli, T. Bendo, C. H. Mello, C. Binder, and A. N. Klein, *Surf. Coat. Technol.* **375**, 911 (2019).
5. G. D. Cui, R. J. Jiang, A. Li, C. S. Zhang, and J. Y. Chen, *Steel Res. Int.* **89**, 1700357 (2017).
6. T. Bendo, A. M. Maliska, J. J. S. Acuña, C. Binder, K. B. Demetrio, and A. N. Klein, *Surf. Coat. Technol.* **258**, 368 (2014).
7. A. Fomin, M. Fomina, V. Koshuro, and I. Rodionov, *Compos. Struct.* **229**, 111451 (2019).
8. W. D. Zhang, G. Q. Zhao, and Q. J. Fu, *Mater. Sci. Eng. A* **736**, 276 (2018).
9. S. Chauhan, V. Verma, U. Prakash, P. C. Tewari, and D. Khanduja, *Int. J. Miner. Metall. Mater.* **24**, 373 (2017).
10. X. L. Wang, Q. S. Meng, Z. Wang, J. Gan, Y. Yang, X. P. Qin, K. Gao, H. L. Zhong, M. Cheng, and X. Y. Gan, *Surf. Coat. Technol.* **357**, 252 (2019).
11. V. Javaheri, S. Kolli, B. Grande, and D. Porter, *Mater. Charact.* **149**, 165 (2019).
12. J. Montalvo-Urquizo, Q. Liu, and A. Schmidt, *Comput. Mater. Sci.* **79**, 639 (2013).
13. R. Naar and F. Bay, *Appl. Math. Model.* **37**, 2074 (2013).
14. Y. Han, E. Yu, H. Zhang, and D. C. Huang, *Appl. Therm. Eng.* **51**, 212 (2013).
15. G. D. Cui, X. Wei, E. A. Olevsky, R. M. German, and J. Y. Chen, *Mater. Des.* **90**, 115 (2016).
16. R. J. Brook, *J. Am. Ceram. Soc.* **52**, 56 (1969).
17. Y. S. Zou, H. Z. Gu, A. Huang, L. P. Fu, and G. Q. Li, *Mater. Des.* **186**, 108326 (2020).
18. S. E. Offerman, V. Dijk, J. Sietsma, V. D. Zwaag, E. M. Lauridsen, L. Margulies, S. Grigull, and H. F. Poulsen, *Scr. Mater.* **51**, 937 (2004).
19. Y. Xu, D. Casari, D. Qiang, R. H. Mathiesen, L. Arnborg, and Y. J. Li, *Acta Mater.* **140**, 224 (2017).
20. W. Qi, Y. Peng, Y. Han, R. K. Bowles, and M. Dijkstra, *Phys. Rev. Lett.* **115**, 185701 (2015).
21. Z. Q. Li, D. K. Wang, and D. Y. Song, *J. China Coal Soc.* **40**, 1055 (2015).
22. J. Li, Z. Wang, and F. L. Deepak, *ACS Nano* **11**, 5590 (2017).
23. B. Zhang, F. Xue, S. L. Li, X. T. Wang, N. N. Liang, Y. H. Zhao, and G. Sha, *Acta Mater.* **140**, 388 (2017).
24. R. M. German, *Sintering: From Empirical Observations to Scientific Principles* (Elsevier, Amsterdam, 2014).
25. D. Tabor, *The Hardness of Metals* (Clarendon, Oxford, 1951).
26. M. Y. Seo, I. C. Choi, J. Moon, S. Kim, U. Ramamurthy, and J. Jiang, *Scr. Mater.* **87**, 49 (2014).
27. K. Durst, B. Backes, O. Franke, and M. Göken, *Acta Mater.* **54**, 2547 (2006).
28. E. Hernández-Nava, C. J. Smith, F. Derguti, S. Tammas-Williams, F. Léonard, P. J. Withers, I. Todd, and R. Goodall, *Acta Mater.* **85**, 387 (2015).
29. Y. S. Zou, H. Z. Gu, A. Huang, L. P. Fu, and G. Q. Li, *Mater. Des.* **186**, 108326 (2020).